Heat- and light-induced transformations of Yb trapping sites in an Ar matrix

L.-G. Tao, N. N. Kleshchina, R. Lambo, A. A. Buchachenko, X.-G. Zhou, D. S. Bezrukov, and S.-M. Hu

Citation: The Journal of Chemical Physics **143**, 174306 (2015); doi: 10.1063/1.4934999
View online: http://dx.doi.org/10.1063/1.4934999
View Table of Contents: http://scitation.aip.org/content/aip/journal/jcp/143/17?ver=pdfcov
Published by the AIP Publishing

Heat- and light-induced transformations of Yb trapping sites in an Ar matrix

L.-G. Tao,[1] N. N. Kleshchina,[2] R. Lambo,[1,a)] A. A. Buchachenko,[3,b)] X.-G. Zhou,[1] D. S. Bezrukov,[2] and S.-M. Hu[1]

[1]*Hefei National Laboratory for Physical Sciences at the Microscale, Collaborative Innovation Center of Chemistry for Energy Materials, University of Science and Technology of China, Hefei 230026, China*
[2]*Department of Chemistry, M. V. Lomonosov Moscow State University, Moscow 119991, Russia*
[3]*Skolkovo Institute of Science and Technology, 100 Novaya St., Skolkovo, Moscow Region 143025, Russia*

(Received 7 March 2015; accepted 19 October 2015; published online 6 November 2015)

The low-lying electronic states of Yb isolated in a solid Ar matrix grown at 4.2 K are characterized through absorption and emission spectroscopy. Yb atoms are found to occupy three distinct thermally stable trapping sites labeled "red," "blue," and "violet" according to the relative positions of the absorption features they produce. Classical simulations of the site structure and relative stability broadly reproduced the experimentally observed matrix-induced frequency shifts and thus identified the red, blue, and violet sites as due to respective single substitutional (ss), tetravacancy (TV), and hexavacancy (HV) occupation. Prolonged excitation of the $^1S \rightarrow {}^1P$ transition was found to transfer the Yb population from HV sites into TV and ss sites. The process showed reversibility in that annealing to 24 K predominantly transferred the TV population back into HV sites. Population kinetics were used to deduce the effective rate parameters for the site transformation processes. Experimental observations indicate that the blue and violet sites lie close in energy, whereas the red one is much less stable. Classical simulations identify the blue site as the most stable one. © *2015 AIP Publishing LLC.* [http://dx.doi.org/10.1063/1.4934999]

I. INTRODUCTION

Experimental and theoretical work on the multiple trapping sites occupied by metal (M) atoms isolated in rare gas (RG) matrices have largely focused on alkalis such as Li,[1] K,[2] and Rb.[3] These species are attractive to the experimentalist because they possess strong S → P transitions amenable to excitation in the UV-visible range. Spectroscopy of their M/RG systems has revealed that each allowed transition can produce at least two absorption peaks, typically a lower frequency one corresponding to occupation in a "red" trapping site and a higher frequency one corresponding to occupation in a "blue" trapping site. In the cases for which accurate M · RG interaction potentials are available, core polarization pseudopotentials[4] or molecular dynamics[5] calculations have been used to identify these trapping sites as one-, four-, or six-atom vacancies in the RG crystal.

In comparison, studies of multiple site occupation by non-alkali atoms have been limited. To date, the only other species found to occupy pairs of thermally stable sites are Mn[6,7] and Eu[8,9] in solid Ar and Kr. Earlier work on another lanthanide in isolation, Yb, mentions that "absorption bands may be broadened and/or further split due to inhomogeneity of matrix sites."[10] However, it does not positively identify the number and symmetries of these sites. This is likely because the deposition of Yb was performed using laser ablation at high temperature (20 K) to encourage dimer formation. The contribution of higher aggregates to the linewidth of the absorption bands would have obscured the signals of the Yb atom in multiple trapping sites.

The present work re-examines the trapping sites of Yb isolated in thin Ar films by thermal deposition using standard absorption and emission spectroscopy. The combined picture offered by these two spectra indicates the existence of three distinct stable trapping sites designated as "violet," "blue," and "red." To provide interpretation for these results, we also carried out classical simulations of the trapping sites based on the *ab initio* Yb · Ar interaction potentials. Simulated structures and associated $^1S \rightarrow {}^1P$ transition frequencies allowed us to assign tentatively the violet, blue, and red sites to Yb atoms trapped in hexavacancy (HV), tetravacancy (TV), and single-substitution (ss) sites, respectively.

We also find evidence that these sites can be transformed from one kind into another by annealing and irradiation. To our knowledge, the only systems for which both heat- and light-induced atomic migration have been previously demonstrated are K/Ar[11] and Ag/Xe.[12] In both cases, excitation of the principal transition stimulates the migration of the M atom from occupation in a thermally stable trapping site to occupation in a metastable trapping site. The latter site manifests itself as a distinct, redshifted band whose formation obeys simple first order kinetics. This process was found to be reversible, so that annealing nearly completely restored the atomic population to its original trapping site with small losses due to dimerization.

By contrast, our present observations evidence population transfers between the stable trapping sites. We found that prolonged excitation of the Yb/Ar singlet transition efficiently transfers the atomic population from violet to blue and red sites at low temperature. The process showed good reversibility on annealing with the violet sites being repopulated out of the blue

a)Electronic mail: lambo@mail.ustc.edu.cn
b)Electronic mail: a.buchachenko@skoltech.ru

ones. The relative stability of the distinct sites, blue ≈ violet ≫ red, inferred from these observations, agrees well with the results of the classical simulations that predict a TV > HV ≫ SS stability order.

The remainder of this paper is organized as follows: In Section II, experimental methods and results are presented, while Section III gives a brief account of the simulations. Experimental and theoretical findings are discussed together in Section IV with conclusions presented in Section V.

II. EXPERIMENT

A. Setup

The principal components of the experimental setup were the same as those used by our group in earlier experiments.[13] A 1 in. diameter BaF_2 window was chosen as the substrate on which to grow the matrix and thermally anchored to the coldhead of a closed-cycle helium refrigerator (Janis SHI-4-5) in a sample chamber evacuated to a pressure of 10^{-5} Pa. The substrate was thus maintained at a base temperature of 4.2 K during crystal growth. The matrix itself was prepared by co-depositing a small Ar flux together with a Yb atomic beam produced by a Knudsen effusion oven. The oven temperature was set to 395 °C and a gas flux of 0.45 SCCM was maintained by a mass flow controller (MKS 1479 A). Samples prepared for absorption spectroscopy were grown over 10-15 min, while those prepared for the emission spectroscopy were grown over approximately 2 h.

A Thorlabs CCS 2000 spectrometer capable of a resolution of 0.5 nm was used to record the results of UV-visible excitation. Continuous white-light absorption spectra were obtained using emission from a Xe lamp passing directly through the matrix. Emission spectra were measured perpendicular to the matrix following excitation by a dye laser (Sirah PRSC-LG-24) pumped by the third harmonic (355 nm) of a Nd:YAG laser (Spectra Physics PRO-190). The Nd:YAG pump produced a pulse with a FWHM of 8 ns at a rate of 10 Hz, and laser radiation of approximately 400-600 μJ/pulse was obtained in the frequency range associated with a mixed dye of Exalite 389 and 398 (388-403 nm). A high power light emitting diode (LED) with a broad linewidth (~5 nm) centered at 390 nm was used as a second optical pump.

The temperature of the system was monitored using a silicon diode sensor (DT-470) mounted on the baseplate holding the substrate and read off a temperature controller (Lake Shore 331S). A resistive heater mounted on the coldhead and controlled by a PID loop allowed us to stabilize the temperature of the BaF_2 window to within 0.2 K between 4.2 K and 40 K during annealing cycles.

B. Absorption spectra

The diagram of the relevant low-lying energy levels and transitions between them for the Yb atom in the gas-phase[14] is presented in Figure 1.

The UV-visible absorption spectra of the Yb/Ar sample are shown in Figure 2. (The absorbance, A, is calculated as $A = \log_{10}(I_0/I)$, where the intensity of the probe beam at each frequency with and without the sample is given by I and I_0, respectively.) Two large spectral features can be readily seen: one in the 336-354 nm range and another in the 381-411 nm range. The atomic transitions nearest in frequency to these features are, respectively, the $6s^2\ ^1S_0 \rightarrow 4f^{13}5d6s^2$ and $6s^2\ ^1S_0 \rightarrow 6s6p\ ^1P_1$ transitions.

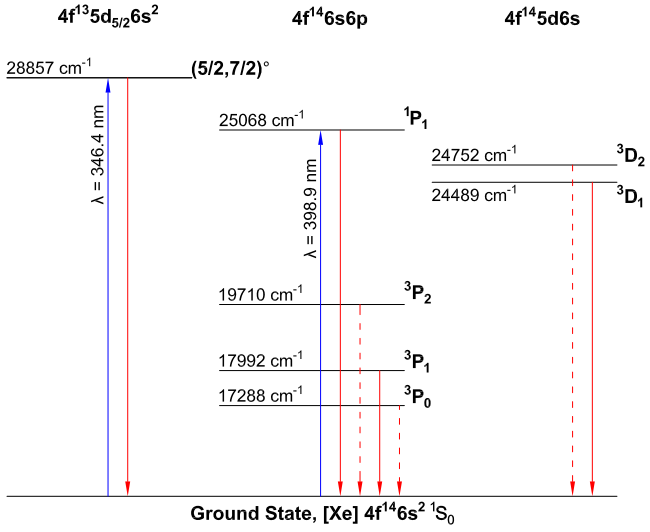

FIG. 1. Diagram of the relevant low-lying electronic energy levels of the Yb atom in a gas phase.[14] The transitions with the strongest absorption oscillator strength are indicated by blue upward arrows. The transitions relevant to the Yb/RG emission spectra are indicated by the red downward arrows.

These absorption bands show certain finer structures that are explained as due to the presence of Yb atoms in different Ar trapping sites. In the unannealed sample, the features at 390 nm and 394 nm are assigned to the $6s^2\ ^1S_0 \rightarrow 6s6p\ ^1P_1$ transition of the Yb atom under respective "violet" and "blue" site occupation. A shoulder at lower frequency, beginning at 401 nm and extending to 411 nm, also indicates the presence of a small Yb population in a third "red" trapping site. Similarly,

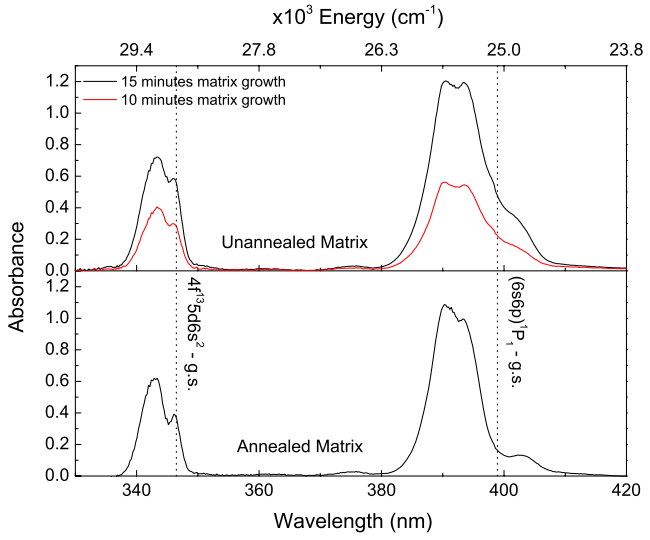

FIG. 2. White-light normalized absorption spectra showing the peaks assigned to the $6s^2\ ^1S_0 \rightarrow 4f^{13}5d6s^2$ and $6s^2\ ^1S_0 \rightarrow 6s6p\ ^1P_1$ transitions. The red and black traces in the top panel show the results of matrix growth at 4.2 K for 10 and 15 min. The bottom trace shows the result of annealing the latter to 24 K for 15 min.

TABLE I. Principal features of the absorption spectra of the annealed Yb/Ar system. Here, λ and ν refer, respectively, to the wavelength and transition frequency; δ refers to the matrix frequency shift relative to the gas phase transition frequency. An uncertainty of ±40 cm^{-1} is assumed on all values.

Transition	λ (nm)	ν (cm^{-1})	δ (cm^{-1})
	Yb/Ar red site		
$6s^2\ ^1S_0 \rightarrow 6s6p\ ^1P_1$	403.4	24 785	−284
	Yb/Ar blue site		
$6s^2\ ^1S_0 \rightarrow 4f^{13}5d6s^2$	346.1	28 892	36
$6s^2\ ^1S_0 \rightarrow 6s6p\ ^1P_1$	393.5	25 413	345
	Yb/Ar violet site		
$6s^2\ ^1S_0 \rightarrow 4f^{13}5d6s^2$	343.1	29 146	289
$6s^2\ ^1S_0 \rightarrow 6s6p\ ^1P_1$	390.0	25 641	572

the peaks at 344 nm and 347 nm are assigned to the $6s^2\ ^1S_0 \rightarrow 4f^{13}5d6s^2$ transition of the Yb atom occupying, respectively, a violet and a blue site. However, in part because of the weaker dipole oscillator strength of the latter transition, no structure corresponding to the red shoulder of the singlet transition is easily identifiable at higher frequency.

The spectrum in the bottom panel of Fig. 2 shows the results of annealing to 24 K for 15 min. The features assigned to the blue and violet sites survive, while that assigned to the red site becomes more clearly visible with its peak shifted to 403 nm. The fact that all three features withstand annealing attests to the stability of the corresponding sites. One should also note a small change in the relative amplitudes of the remaining features with the violet peak becoming more pronounced at the expense of the blue peak.

The observed absorption spectral features are characterized in Table I. We note that the absorption spectrum of the Yb/Ar system is different from that of the Yb/Ne one, in which the same $6s^2\ ^1S_0 \rightarrow 4f^{13}5d6s^2$ and $6s^2\ ^1S_0 \rightarrow 6s6p\ ^1P_1$ transitions each produced single, structureless absorption bands. Furthermore, annealing had no effect on the lineshapes of the bands in solid Ne, whereas in solid Ar it produced a clearer discrimination of the three-fold structure.

C. $6s^2\ ^1S_0 \rightarrow 6s6p\ ^1P_1$ emission spectra

Emission spectra were first recorded from Yb/Ar samples using the pulsed dye laser to excite the $6s^2\ ^1S_0 \rightarrow 6s6p\ ^1P_1$ transition. The spectra obtained with the laser at 391 nm are shown in Figure 3. Almost all of the emission is concentrated in the spectral region of the $6s6p\ ^3P_1$ state and consists of two strong bands centered at 544 and 569 nm and a weak feature at 600 nm, as characterized in Table II. This three-fold structure resembles that observed in the spectra of the Yb/Ne system, whose emission is less blue-shifted, but still dominated by the singlet component of the $6s6p\ ^3P_J$ manifold.[13] However, the origins of such structures turn out to be different for the two systems.

Figure 3 reveals a pronounced variation in the relative emission intensities of the three features upon annealing and matrix irradiation not seen in the Yb/Ne system.[13] For this reason, the structure of Yb/Ne emission spectra was assigned

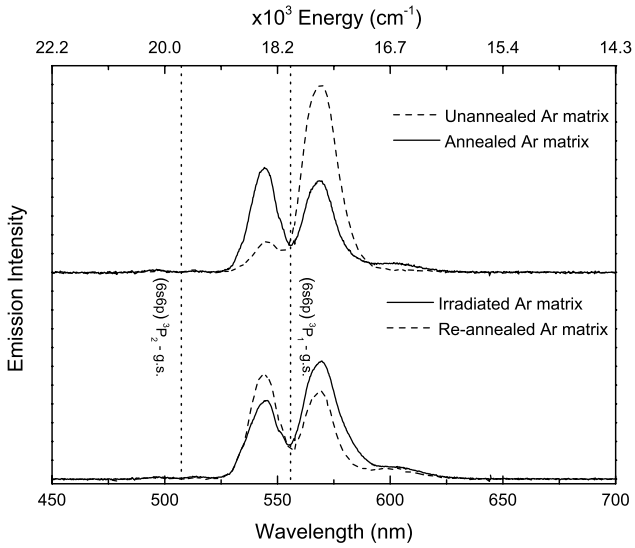

FIG. 3. Emission spectra of the Yb/Ar system excited with a laser centered at 391 nm. The top panel shows the difference between an unannealed (dashed line) and annealed (solid line) sample. The bottom panel shows the effects of irradiation for 3 min (solid line) on the latter sample and that of subsequent re-annealing (dashed line).

to transitions from distinct electronic states. Indeed, lifetime measurements allowed us to assign three Yb/Ne emission features to the $6p^2\ ^3P_1 \rightarrow 6s6p\ ^1P_1$, $6s6p\ ^3P_1 \rightarrow 6s^2\ ^1S_0$, and $6s6p\ ^3P_0 \rightarrow 6s^2\ ^1S_0$ transitions, in order of increasing wavelength.[13]

The lifetimes of the Yb($^3P_1$) state in RG matrices have been recently measured by the Argonne group.[15] It was found that the Yb/Ar emission, averaged with the intensity profile over the 543-600 nm range, decays exponentially at a rate of $1.8 \times 10^6\ s^{-1}$, close to the gas-phase value of $1.16 \times 10^6\ s^{-1}$.[16] Moreover, attempts have been made to identify the emission from the metastable Yb $^3P_0$ or $^3P_2$ states.[17] A long-lived emission feature with a lifetime on the order of 7 s was identified at 566 nm with an intensity ten times smaller than that of the dominant 544 nm emission peak. This feature is completely masked by the 569 nm peak at steady

TABLE II. Principal features of the emission spectrum for the annealed Yb/Ar system resulting from $6s^2\ ^1S_0 \rightarrow 6s6p\ ^1P_1$ excitation. The symbols here are the same as those used in Table I. Here, L and D refer to the results of excitation using the 391 nm laser and the 390 nm LED, respectively, while Δ refers to the transition linewidth (FWHM). The uncertainty is assumed to be ±40 cm^{-1} on all values.

Transition		λ (nm)	ν (cm^{-1})	Δ (cm^{-1})	δ (cm^{-1})
		Yb/Ar red site			
$6s6p\ ^3P_1 \rightarrow 6s^2\ ^1S_0$	L	600.6	16 650	700	−1342
	D	600.0	16 669	700	−1323
		Yb/Ar blue site			
$6s6p\ ^3P_1 \rightarrow 6s^2\ ^1S_0$	L	568.8	17 581	490	−411
	D	569.0	17 574	440	−418
		Yb/Ar violet site			
$6s6p\ ^3P_1 \rightarrow 6s^2\ ^1S_0$	L	544.2	18 376	480	384
	D	543.5	18 400	380	408

state excitation conditions and can only be distinguished after shutting down the excitation source. These observations preclude the assignment of any of the three Yb/Ar emission features to a transition other than the $6s6p\ ^3P_1 \rightarrow 6s^2\ ^1S_0$ one and support their attribution to distinct trapping sites.

Another difference between the two matrices is that the minor $^1P_1$ and $^3D_{1,2}$ emissions observed in the Yb/Ne one at wavelengths below 410 nm[13] were not detected in that of Yb/Ar. It is reasonable to assume that stronger perturbation by the heavier host makes intersystem crossing more efficient to fully quench the singlet emission and, perhaps, the emission from the ^3D_J manifold.

The results presented in Figure 3 show the remarkable effect of annealing on the emission spectra. The dashed line in the upper panel shows that the Yb population in the unannealed sample is largely concentrated in the blue sites (569 nm). Annealing to 24 K for 15 min (without irradiation) redistributes the population towards the violet (544 nm) and, to some extent, the red (600 nm) sites. The solid line in the bottom panel shows that exposure to radiation (~3 min) reverses this behavior, predominantly transferring the violet population into the blue one. Re-annealing the sample at 24 K (without irradiation) again encourages the redistribution of the blue population restoring initial violet and red site occupations.

It was observed that both heat and light effects are reversible and could be repeated numerous times. The natural factors limiting the cycling are the evaporation of the matrix and some losses due to Yb_n cluster formation. Thus, successive cycles of annealing and irradiation uniformly decrease the absolute amplitudes of the three peaks, but preserve their relative intensities.

These findings can be interpreted as the transformation of the Yb/Ar trapping sites due to Yb atom migration and/or local restructuring of the matrix environment. To study site transformations more carefully, we used continuous radiation from a high-power LED. We first checked that the emission spectra obtained with a 390 nm LED were very similar to those recorded with a 391 nm laser (Fig. 3), as compared in Table II. Likewise, the variations of the spectra under annealing and irradiation were found to be the same for the two excitation sources.

We analyzed the evolution of the emission spectra in the course of heating an unannealed sample using the 390 nm LED. Figure 4 shows the variation of the amplitudes of the violet (544 nm), blue (568 nm), and red (600 nm) peaks in time. The resistive heater effectively increased the temperature of the sample in stages from 4.5 K to 8 K, 16 K to 21 K. At the onset of each stage, there is a decrease in the amplitude of the blue site population until it reaches a new equilibrium with the flux of atoms from violet and red sites. A low light level (~0.2 mW/cm^2) was used to minimize light-induced activity. Nonetheless, because of the backflow into blue sites, the heat-induced transfer process is noticeably less efficient in the presence of light.

III. CLASSICAL SIMULATIONS

To interpret the experimental findings, we used the original classical model that describes the accommodation of Yb

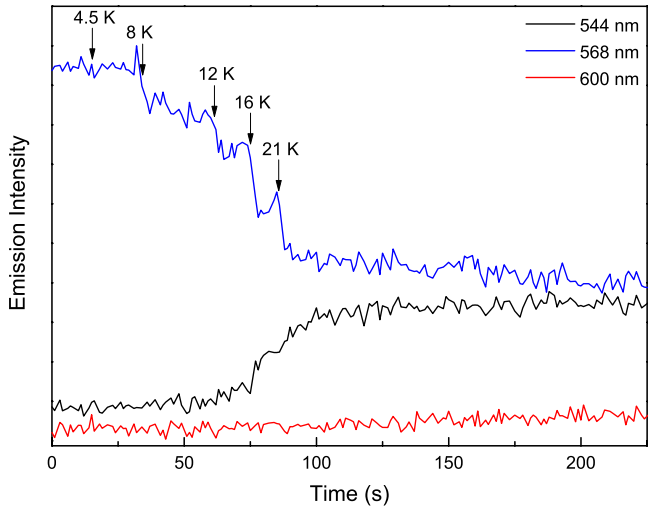

FIG. 4. Variation of the amplitudes of the emission peaks produced by continuous LED excitation at 390 nm during an annealing cycle. The temperature of the sample at the onset of various points during the cycle is indicated by the black arrows.

atoms in an inert matrix. Detailed presentation of the model, which is still under development and testing, is reserved for forthcoming publications. Only the basic features are presented here to justify its results.

A. The model

The model assumes a pairwise potential approximation. Its starting point is an infinite ideal Ar *fcc* lattice with the lattice parameter a, in which we define two concentric spheres with the radii R_A and R_B, $R_A < R_B$. The former sphere encloses N_A Ar atoms and forms subsystem A. The latter sphere defines subsystem B, which contains N_B Ar atoms with the distances from the origin lying between R_A and R_B. They are always kept fixed at the ideal lattice sites to maintain a potential field reflecting the long-range order of the crystal. All the subsequent manipulations are made within the subsystem A, while the target quantity is the composite energy

$$E_c = E_A + E_B + E_{AB}, \tag{1}$$

where E_A and E_B are the potential energies of interaction of atoms belonging to subsystems A and B, respectively, and E_{AB} accounts for interactions of atoms belonging to distinct subsystems. Minimization of E_c in the coordinate space of subsystem A defines the stable structure(s). Note that E_B term is always constant and can be omitted.

First, the Yb atom is placed at the origin and composite energy is minimized with respect to coordinates of all Ar atoms within the sphere A to give the most stable configuration with the energy $E_c(0)$. Then, n Ar atoms from the Yb neighborhood are removed and the most stable configuration with energy $E_c(n)$ is found. The energies $E_c(n)$ characterize the system with different numbers of atoms, $N_A + N_B - n$. To relate them to the common origin, we consider the formation of the atomic vacancy in subsystem A as a virtual process in which an atom is moved out of the system encircled by sphere B to the rest of the infinite lattice. In its final state, an atom does not influence E_c,

whereas its initial contribution to E_c was E_{at} (atomization energy per atom taken with a negative sign and equal to half of the interaction energy of an atom with all others). Assuming that this correction is additive in n, the dependence of the corrected energies on the number of removed atoms n is given simply by $E(n) = E_c(n) - nE_{at}$ and features the relative stability of the site structure in a similar way to the convex hull concept in the phase diagrams of multicomponent systems.[18]

Special care was taken to guarantee that at each n the lowest-energy structure is found. In addition to brute-force Monte-Carlo sampling, we used simulated annealing[19] and a kind of genealogical sampling, in which the starting configurations for nth step are generated by removing atoms from stable configurations found in the $(n-1)$th step. All three approaches gave the same result at least up to $n = 12$.

To link the predicted structures with absorption spectrum features, we estimated vertical energies of the Yb(^{1}S) → Yb(^{1}P) transition using the diatomics-in-molecule (DIM) prescription, see, e.g., Ref. 5.

B. Pairwise potentials

The ground-state potential energy was approximated as the sum of pairwise potential functions for Yb(^{1}S) · Ar $^1\Sigma^+$ and Ar · Ar interactions.

For the former, we used *ab initio* results obtained as described in Ref. 13 for Yb · Ne. In brief, the Yb atom was described with the ECP28MDF effective core potential and the supplementary basis set[20] further expanded by adding the set of spdfg primitives continuing the smallest exponents in each symmetry type as an even-tempered sequence. For Ar, augmented correlation consistent polarized quadruple-zeta basis set aug-cc-pVQZ[21] was employed. To further saturate dispersion interaction, the 3s3p2d2f1g set of bond functions[22] was added in the middle of the internuclear distance. The potentials were obtained by the single-reference coupled cluster calculations implemented here with singles, doubles, and non-iterative correction to triples, CCSD(T),[23,24] with Yb($4s^24p^64d^{10}$), Ar($1s^22s^22p^6$) shells kept in core and counterpoise correction[25] included.

Three excited scalar-relativistic DIM potential energy surfaces are expressed as the angle-dependent combinations of Yb(^{1}P) · Ar $2^1\Sigma^+$ and $1^1\Pi$ interaction potentials with the sum of Ar · Ar interactions added, in full analogy with the Na(^{2}P) · Ar case.[5] Excited-state potentials were calculated using the multireference configuration interaction (MRCI) technique.[26] For Yb, the ECP28MWB effective core potential[27] was implemented in combination with the segmented basis[28] augmented by the s2pdfg diffuse primitive set.[29] The Ar atom was treated as described above. The active space consisted of orbitals correlating to the Yb(6s,6p,6d) and Ar(3p) shells, while the Yb($4f^{14}$) shell was correlated as fully occupied. Computed excitation energies were added to the ground-state CCSD(T) potentials and adjusted, asymptotically, to the measured ^{1}P term value.[14] All calculations were performed using the MOLPRO program package.[30]

Ab initio points were fit to the exponential-spline-van der Waals form. The same form was used, for consistency, for the Ar · Ar potential borrowed from Aziz and co-workers.[31]

C. Site structure, stability, and assignment

Figure 5 shows the interaction potentials used in the simulations plotted with respect to the common zero of energy at the dissociation limit. The interaction of the ground-state Yb atom with Ar is weaker than the Ar · Ar interaction: replacement of Ar by Yb reduces the binding energy from 100 to 70 cm^{-1} and stretches the equilibrium distance from 3.76 to 5.03 Å. Excitation of Yb to the ^{1}P state gives two distinct potentials, almost repulsive $2^1\Sigma^+$ and bound flat $^1\Pi$ ones. A similar picture was observed for the Na(^{2}S, ^{2}P) · Ar interaction,[5] except with much larger splitting between excited Σ and Π potentials.

Using our potential model, we obtained, for an ideal Ar crystal, the lattice parameter $a = 5.200$ Å and $E_{at} = -783$ cm^{-1}. These values are 2% and 21% off the measured ones, 5.311 Å[32] and −646 cm^{-1},[33] respectively. According to a thorough *ab initio* study in Ref. 34, such accuracy is close to the limit of the classical pairwise approximation: contributions of three- and four-body interactions, as well as the effect of the zero-point energy, amount to 2% and 18% of a and E_{at}, respectively, and bring these quantities into excellent agreement with experiment. In all subsequent calculations, the optimized parameters are used. Preliminary tests indicated that the simulations converge at $R_A = 3a$ and $R_B = 8a$ ($N_A \approx 400$, $N_B \approx 7500$ Ar atoms).

Figure 6 shows our results for $E(n)$, energy of the most stable structure found for Yb trapped in the system with n atoms removed. It identifies three features, a "global" minimum at $n = 4$, a "local" minimum at $n = 6$, and a "shoulder" at $n = 1$. We interpret them as the distinct trapping sites in the sense of convex hull analysis, as the points of the "phase diagram" Yb · $(N_A - n)$Ar that lie below the line connecting Yb · $(N_A - n - 1)$Ar and Yb · $(N_A - n + 1)$Ar points.

All three structures are perfectly symmetric and correspond to the Yb atom accommodated in the tetrahedral ($n = 4$) or octahedral ($n = 6$) *fcc* vacancies or placed instead of one lattice atom ($n = 1$), i.e., to TV, HV, and SS trapping sites. Schematic structures of these sites are presented in Figure 6. Table III compares the geometries of the trapping sites found with those of an ideal *fcc* lattice in terms of the distances

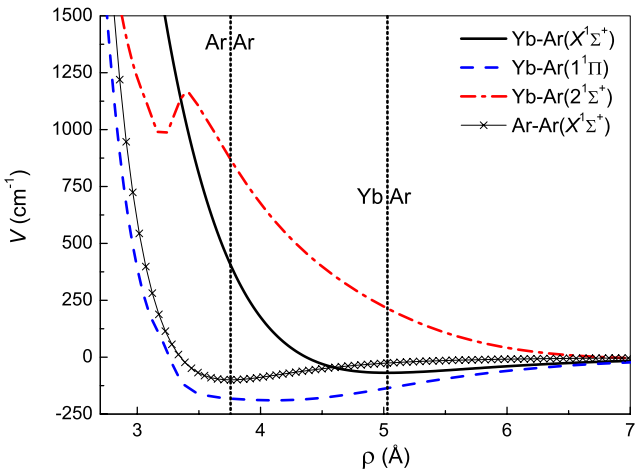

FIG. 5. Potentials of Yb(^{1}S), Yb(^{1}P), and Ar interactions with Ar atom plotted with respect to a common dissociation limit. Vertical lines mark the equilibrium distances of the ground-state Yb · Ar and Ar · Ar potentials.

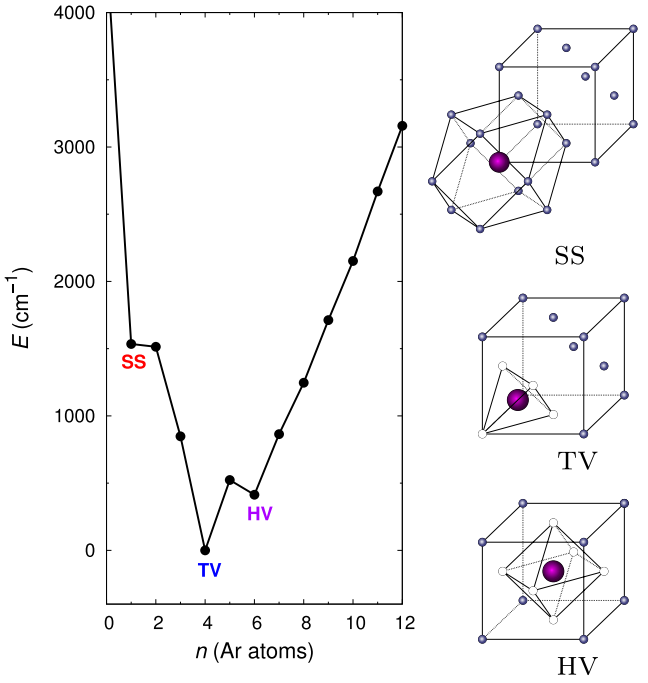

FIG. 6. Energies of the most stable structures found for Yb atom embedded in the system with n Ar atoms removed. The zero of energy is referred to the lowest $n = 4$ structure. Also shown are the structures of the Yb trapping sites with Yb atom represented by large sphere, removed Ar atoms—by white circles, and Ar atoms—by small spheres. Structure of the SS site is shown with a polyhedron formed by the first coordination shell of Yb, while the polyhedra formed by removed Ar atoms are drawn in the structures of the TV and HV sites.

between the Yb (or equivalent Ar atom) and the Ar atoms forming the first three coordination shells $i = 1, 2, 3$. The effective volume occupied by Yb grows along the SS, TV, and HV sequence, but the minimum Yb–Ar distance is always significantly shorter (by 20%, 12%, and 10%, respectively) than the equilibrium distance in the Yb · Ar dimer. The mismatch in the Yb · Ar and Ar · Ar interaction range leads to remarkable swelling of the nearest coordination shell, in part compensated by slight contraction of the next shell, with respect to an ideal Ar lattice. The relative stability of the trapping sites can be inferred from the $E(n)$ dependence in Fig. 6: TV site is the most stable, whereas HV and SS sites lie ca. 400 and 1500 cm^{-1} higher, respectively.

Due to high symmetry, each of the three structures gives the single vertical transition to the states associated with $^1S \rightarrow {}^1P$ excitation of the trapped Yb. Their shifts from the gas-phase frequency are estimated as −473, 612, and 697 cm^{-1} for SS, TV, and HV sites, respectively. These values are in qualitative agreement with the shifts of observed transitions (see Table I) and allow us to tentatively identify observed absorption bands with the trapping sites of specific symmetries, namely, violet with HV, blue with TV, and red with SS.

TABLE III. Distances from Ar or Yb atom to n_i Ar atoms forming ith coordination shell in the ideal *fcc* lattice ($a = 5.200$ Å) or in the optimized Yb trapping sites, in Å.

i	n_i	Ideal *fcc*	Yb in Ar
		Single substitution (SS)	
1	12	3.68	4.04
2	6	5.20	5.19
3	24	6.37	6.48
		Tetravacancy (TV)	
1	4	2.25	…[a]
2	12	4.31	4.42
3	12	5.67	5.64
		Hexavacancy (HV)	
1	6	2.60	…[a]
2	8	4.50	4.54
3	24	5.82	5.79

[a]Shell removed to accommodate Yb atom.

IV. DISCUSSION

A. Matrix trapping sites

The work of Jeong and Klabunde[35] has shown the matrix-induced frequency shifts to depend on the strength of M·RG van der Waals interactions which increase in the heavier, more polarizable RG hosts. Subsequent work by Laursen and Cartland[36] demonstrated that the relationship between the matrix shift (δ) seen in the S → P transitions is approximately linear with the polarizability of the matrix host.

Figure 7 shows the plots of the matrix shift against the polarizability of RG atom for the singlet transition of Yb in isolation. The trend observed for the blue sites in the RGs indicates that they have the same structure. Previously published data for Ne[13] have been plotted to show that the dominant trapping site also follows the same trend. These results compare reasonably well to those obtained using laser ablation to deposit the Yb atoms,[10] which suggests that this technique promotes isolation primarily in the same blue sites. Meanwhile, the red and violet sites in the Ar matrix are far off the blue site trend line, reflecting the fact that they have different symmetries.

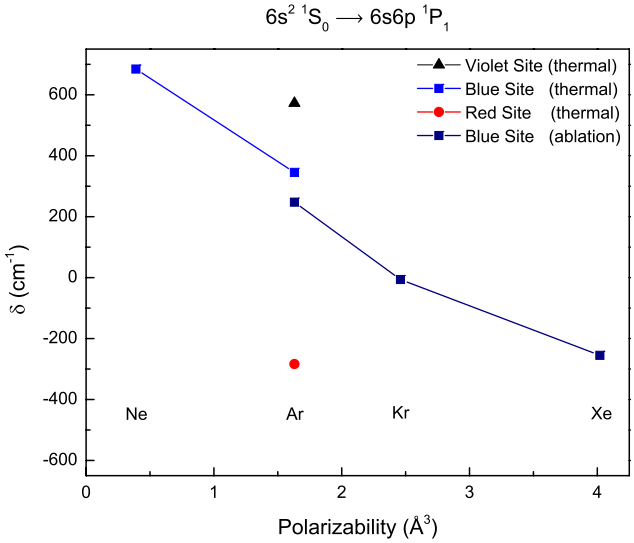

FIG. 7. Plot of the frequency shift (δ cm^{-1}) of the $6s^2\ {}^1S_0 \rightarrow 6s6p\ {}^1P_1$ transition against polarizability for each matrix host. The data obtained by thermal deposition of Yb atoms by our group are compared to that obtained by ablation deposition techniques in previously published works.[10]

The matrix-isolated Eu atom, which differs from the Yb atom in its 4f shell occupation (7 unpaired electrons vs. 14 paired ones), has been thoroughly investigated by Byrne and McCaffrey[8,9,37] and offers an interesting point of comparison. In solid Ar, Eu was found to occupy two stable trapping sites, "red" and "blue," with mean frequency shifts of 760 and 1350 cm^{-1}, respectively, in the $6s^2\ ^8S \rightarrow 6s6p\ y^8P$ transition. These shifts are significantly larger than those observed here for the same $6s^2 \rightarrow 6s6p$ electron promotion in the Yb/Ar blue and violet sites (Table I). Considering the volume of the vacancies in the ideal Ar lattice and exploring an analogy to the Na/Ar system, the authors of Ref. 8 attributed the more stable Eu red site to a HV structure and the less stable blue one to a TV structure. If Eu/Ar red and blue sites are linked to Yb/Ar blue and violet sites, respectively, as frequency shift and stability suggest, then this attribution is the opposite of the one argued for Yb/Ar here within a more sophisticated classical model.

For completeness, the observation of two trapping sites of atomic Ho isolated in Ar[38] is worth mentioning, although due to the complexity of the spectra the symmetries of these sites were not investigated. In general, the photophysical properties of the lanthanide atoms in inert matrices should be sensitive to their inner shell structure and may reveal previously unattained effects of the 4f, 5d population on weak interatomic interactions.

B. Model of migration

Site transformation kinetics are usually deduced from the variation of the absorption band intensity upon annealing. In the case of emission spectra, where an excitation source is present, more elaborate analysis is needed to account for population transfers induced by both heat and radiation. To this end, following Schrimpf *et al.*,[11] we demonstrate that a first-order rate equation approach is adequate to quantify the site transformation processes. The numbers of Yb atoms in the violet, blue, and red sites at time t are denoted by $n_v(t)$, $n_b(t)$, and $n_r(t)$, respectively. The rates at which heat- and light-induced processes convert violet site into blue and red ones are denoted by α_b and α_r, respectively. The rates at which these same processes convert blue site into violet and red are denoted by β_v and β_r, respectively. Meanwhile, the rates of backflow from red site to violet and blue sites are denoted by γ_v and γ_b, respectively. The master system of equations describing the above processes is

$$\begin{aligned} \dot{n}_v(t) &= -(\alpha_b + \alpha_r)n_v(t) + \beta_v n_b(t) + \gamma_v n_r(t), \\ \dot{n}_b(t) &= -(\beta_v + \beta_r)n_b(t) + \alpha_b n_v(t) + \gamma_b n_r(t), \\ \dot{n}_r(t) &= -(\gamma_b + \gamma_v)n_r(t) + \alpha_r n_v(t) + \beta_r n_b(t). \end{aligned} \tag{2}$$

In order to use Eq. (2), one needs to obtain the population of each type of site. In the case of strong coupling to matrix phonons, the $6s6p\ ^3P_1$ emission peaks should approach Gaussian distributions.[39] This coupling has effectively been demonstrated for Yb through the measurements of the $^3P_1$ and $^3P_0$ lifetimes in the RGs.[15] We therefore take the populations n_v, n_b, and n_r as proportional to the amplitudes of the $6s6p\ ^3P_1$ violet, blue, and red emission peaks, respectively, further assuming that the overlap between each Gaussian peak is small.

The general solutions for n_v, n_b, and n_r have double exponential forms, which can be considerably simplified when we recall that the red site population is small. We thus take $\gamma_v n_r$ and $\gamma_b n_r$ terms as negligible and concisely express the solutions to the master equation using the hyperbolic functions, $C(x) = \cosh x$ and $S(x) = \sinh x$,

$$\begin{aligned} n_v(t) &= \frac{e^{-lt/2}}{m}\left[mn_v(0)C\left(\frac{mt}{2}\right) + 2\beta_v n_b(0)S\left(\frac{mt}{2}\right)\right. \\ &\quad \left. + (2\beta_v + 2\beta_r - l)n_v(0)S\left(\frac{mt}{2}\right)\right], \\ n_b(t) &= \frac{e^{-lt/2}}{m}\left[mn_b(0)C\left(\frac{mt}{2}\right) + 2\alpha_b n_v(0)S\left(\frac{mt}{2}\right)\right. \\ &\quad \left. - (2\beta_v + 2\beta_r - l)n_b(0)S\left(\frac{mt}{2}\right)\right], \\ n_r(t) &= n_r(0) + n_v(0) - n_v(t) + n_b(0) - n_b(t), \end{aligned} \tag{3}$$

where $l = \alpha_r + \alpha_b + \beta_r + \beta_v$ and $m^2 = l^2 - 4(\alpha_r\beta_v + \alpha_r\beta_r + \alpha_b\beta_r)$. The above equation was used to fit the data collected at low and high temperatures.

For the low-temperature case, the measurements were taken with an annealed sample at 4.5 K, illuminated by the 390 nm LED at an irradiance of ~0.5 mW/cm^2. In order to obtain a good estimate for the light-induced backflow rate from the blue to the violet site, β_v, the freshly deposited sample was annealed only until the populations of the two sites became nearly equal, $n_v(0) \approx n_b(0)$.

Figure 8 shows the least-squares fits to the amplitudes of the violet, blue, and red emission peaks using Eq. (3), as well as the resulting α_b, α_r, β_v, and β_r values. The relatively large error on α_r is due to the low signal-to-noise ratio of the 600 nm peak amplitude. The largest rate α_b indicates that the transformation of the violet site into the blue one is energetically favorable, though the reverse transformation occurs at the smaller but still comparable rate β_v. Meanwhile, the α_r rate of the transformation from the violet to the red site is at least one order of magnitude smaller, indicating that

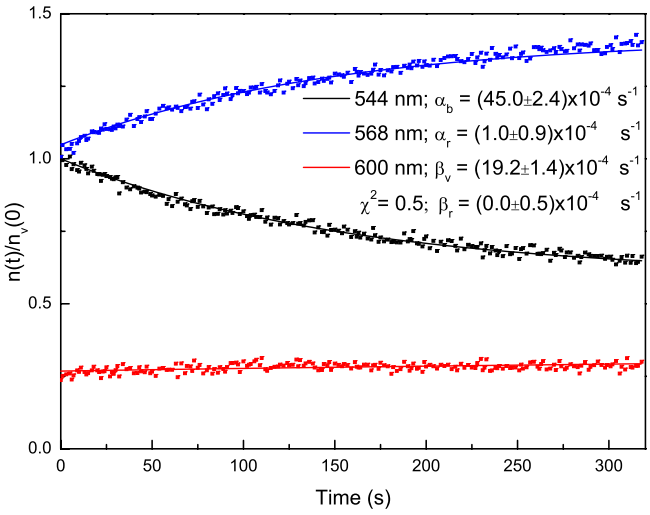

FIG. 8. Least-squares fits of the amplitudes of the emission peaks at 544 nm (middle, black), 568 nm (upper, blue), and 600 nm (lower, red) during exposure to 0.5 mW/cm^2 irradiance at 4.5 K. For clarity, error bars are omitted.

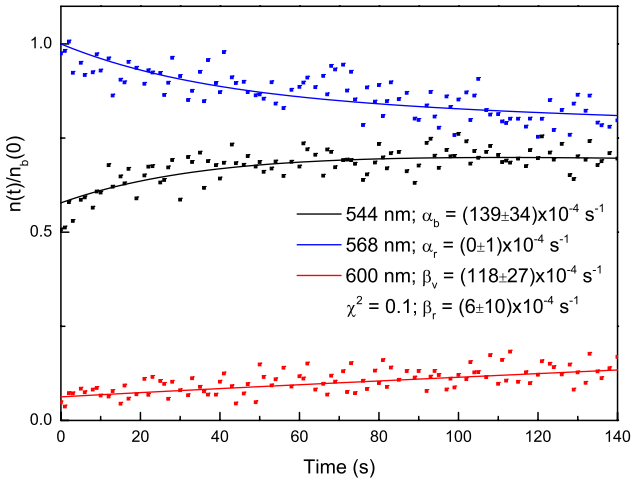

FIG. 9. Least-squares fits of the amplitudes of the emission peaks at 544 nm (middle, black), 568 nm (upper, blue), and 600 nm (lower, red) during exposure to 0.2 mW/cm^2 irradiance at 21 K. For clarity, error bars are omitted.

this process is much less energetically favorable. Attempts to determine the conversion rate of the blue to red site from the least-squares fits gave a value of zero for β_r, suggesting that this site transformation is the least energetically favorable.

Figure 9 shows the least-squares fits using Eq. (3) to the sections of the traces in Figure 4 after 21 K is reached (~85 s). Measurements were taken with an initially unannealed sample illuminated by the 390 nm LED at an irradiance of ~0.2 mW/cm^2.

The high-temperature values of α_b, α_r, β_v, and β_r are given in Figure 9. They generally have larger error bars than the rates measured in the low-temperature regime due to a smaller signal-to-noise ratio at low radiation power. Nonetheless, we observe that the values for β_v and α_b are also significantly higher, in accord with the expected greater mobility of the system at high temperature.

The fit converged to give a value of zero for α_r, suggesting that the rate of transformations of violet sites into red sites is negligible, or at least below the sensitivity of our experiment under these conditions. It should be noted that the lower signal-to-noise ratio at high temperature and the complex interplay of heat and light effects limit the effectiveness of our model in this regime. Nevertheless, the relative order of the rates remains unaltered as the temperature increases: transformation between the blue and violet sites occurs at least an order of magnitude faster than those involving the red site.

C. Site stability

The variation of the absorption bands upon annealing and the site transformation kinetics deduced from the emission spectra provide strong evidence that the red site lies significantly higher in energy than the blue and violet ones. Classical simulations support this conclusion adding further evidence to the identification of the red site with the ss structure.

Under equilibrium, the relation $\alpha_b > \beta_v$ should indicate that the violet site is less stable than the blue one. However, the kinetics deduced from the emission band intensities under irradiation may not be considered as being from an equilibrium state. It features complex relaxation processes occurring in the excited states, which may lead to fast restructuring of the matrix. Indeed, the differences in the excitation and emission frequencies indicate that the amount of energy to be redistributed in non-radiative processes is about 10 000 cm^{-1}. A large fraction may go into the kinetic energy of the Yb atom. The pairwise Yb · Ar potentials change dramatically upon Yb ^{1}S → ^{1}P excitation (cf. Fig. 5) and the ground-state minima may well correspond to the strongly repulsive regions of the excited-state potential energy surface. Furthermore, before emitting from the ^{3}P state, Yb atom undergoes a series of curve-crossing transitions (see discussion in Ref. 13), which may require quite large excursions for less than 5 ns, the radiative lifetime of the ^{1}P state.[40]

Without detailed knowledge of this complicated dynamics, two limiting cases can be hypothesized. The first one assumes that energy relaxation occurs faster than matrix restructuring, i.e., the excited Yb atom maintains its environment unaltered over at least a few ms (as set by the ^{3}P$_1$ radiative lifetime[16]). In this case, observed slow site transformations take place predominantly in the ground state, so that the equilibrium arguments towards higher stability of the blue site are valid. Classical simulations then predict that the violet site lies 400 cm^{-1} above it. In the opposite case, the Yb atom acquires enough kinetic energy to sample a large portion of the excited-state potential energy surface. This suggests the formation of highly delocalized states that sample different initial configurations, so that the emission intensities reflect the excited-state site population transfer rather than the initial ground-state site population distribution. In the extreme in which a single fully delocalized state is formed regardless of the initial conditions, one can estimate the relative energies of the ground-state sites simply as the differences in emission frequencies (Table II): the violet site is the lowest, while the blue and red ones lie 800 cm^{-1} and 1700 cm^{-1} above it, respectively.

The present data do not offer a clear choice between these two pictures. Classical simulations and observation of the single blue site in the previous study using laser ablation[10] point toward the former case. Meanwhile, the data from our absorption spectra may fit both pictures depending on whether one considers the annealed or unannealed sample (see Fig. 2). Though the arguments supporting the first case seem stronger to us, we stick to a conservative conclusion and simply state that the blue TV and the violet HV sites are close in energy.

V. CONCLUSIONS

The photophysical properties of Yb atoms isolated in Ar films were studied by absorption and emission spectroscopy and interpreted with the help of classical simulations. This study led us to a number of conclusions that pointed to similarities and differences with the previously studied Yb/Ne system.[13] For instance, in the Yb/Ar system, emission induced by the 6s^2 ^{1}S$_0$ → 6s6p ^{1}P$_1$ excitation revealed efficient intersystem crossing that completely quenches the singlet state emission and gives rise to the features associated with the 6s6p^{3}P$_1$ → 6s^2 ^{1}S$_0$ transition. However, the absence of emissions from

$^3P_0$, $^3P_2$, and ^3D_J states, that were observed in solid Ne, indicates that non-radiative intersystem transitions are stronger in the Ar matrix.

Furthermore, in contrast to the Yb/Ne case[13] and the previous study of Yb/Ar samples prepared by ablation,[10] our absorption and emission spectra bear clearly resolved structures assignable to three distinct trapping sites, red, blue, and violet, with both the absorption and emission frequencies increasing in the same order. All three sites appear to be stable and reversibly convert to each other by heating or irradiating the sample. An analysis of Yb atom migration in Ar in terms of the site population kinetics deduced from emission spectra indicates strong interrelation of the light- and heat-induced processes. It showed that the blue and violet sites are close in energy, whereas the energy of the red site is significantly higher than that of the other two.

Classical simulations based on the *ab initio* Yb · Ar interaction potentials find three stable structures that correspond to TV, HV, and SS sites of the ideal Ar *fcc* lattice. Accounted for in the simulation is the field due to long-range crystal order, which produces highly symmetric site structures. These structures exhibit significant swelling of the nearest Ar shell and slight contraction of the next shell upon accommodation of Yb. The simulations confirm the higher energy of the SS structure and predict that the HV structure lies only slightly above the TV one in energy. Estimated vertical $6s^2\ ^1S_0 \rightarrow 6s6p\ ^1P_1$ transition frequencies allow us to assign TV, HV, and SS structures to the blue, violet, and red sites, respectively.

To the best of our knowledge, this work represents the first case for which the relative stability of the distinct stable trapping sites has at least been qualitatively assessed by spectroscopic measurements. An important further experiment that can be performed to confirm the picture of the site stability presented here is excitation spectroscopy. It would provide a direct correlation between the features observed in the absorption spectra and those observed in the emission spectra. A longer term prospect for this work would be the investigation of Yb occupation in the heavier RGs. Since the lattice parameter *a* of their crystals is larger, significant differences are expected for multiple site occupation. This should provide a deeper understanding of the process of site transformations of matrix isolated metal atoms. Finally, further improvements of the present classical model should make more direct comparison between experiment and simulations possible.

ACKNOWLEDGMENTS

The authors thank Professor A. Schrimpf for useful discussions and Dr. C.-Y. Xu for sharing his unpublished results in private communications, as well as the referees for their instructive comments. This work has been jointly supported by NSFC (Nos. 21403206 and 21225314), NKBRSF (No. 2013CB834602), and FRFCU. R. Lambo gratefully acknowledges support from the Chinese Academy of Sciences. Part of the work related to classical simulations has been undertaken using the supercomputer facilities of the MSU research computer center and supported by RBRF (Project No. 14-03-00422).

[1]J. J. Wright and L. C. Balling, J. Chem. Phys. **73**, 3103 (1980).
[2]L. C. Balling, M. D. Harvey, and J. J. Wright, J. Chem. Phys. **70**, 2404 (1979).
[3]I. Gerhardt, K. Sin, and T. Momose, J. Chem. Phys. **137**, 014507 (2012).
[4]E. Jacquet, D. Zanuttini, J. Douady, E. Giglio, and B. Gervais, J. Chem. Phys. **135**, 174503 (2011).
[5]M. Ryan, M. Collier, P. de Pujo, C. Crépin, and J. G. McCaffrey, J. Phys. Chem. A **114**, 3011 (2010).
[6]M. A. Collier and J. G. McCaffrey, J. Chem. Phys. **122**, 054503 (2005).
[7]M. A. Collier, O. Byrne, C. Murray, and J. G. McCaffrey, J. Chem. Phys. **132**, 164512 (2010).
[8]O. Byrne and J. G. McCaffrey, J. Chem. Phys. **134**, 124501 (2011).
[9]O. Byrne and J. G. McCaffrey, J. Chem. Phys. **135**, 024507 (2011).
[10]S. Suzer and L. Andrews, J. Chem. Phys. **89**, 5514 (1988).
[11]A. Steinmetz, A. Schrimpf, H.-J. Stöckmann, E. Görlach, R. Dersch, G. Sulzer, and H. Ackermann, Z. Phys. D **4**, 373 (1987).
[12]R. Kometer and N. Schwentner, J. Chem. Phys. **104**, 6967 (1996).
[13]R. Lambo, A. A. Buchachenko, L. Wu, Y. Tan, J. Wang, Y. R. Sun, A.-W. Liu, and S.-M. Hu, J. Chem. Phys. **137**, 204315 (2012).
[14]Yu. Ralchenko, A. E. Kramida, J. Reader, and NIST ASD Team, NIST Atomic Spectra Database, version 4.0.1, National Institute of Standards and Technology, 2010. Available online http://physics.nist.gov/asd.
[15]C.-Y. Xu, J. Singh, K. G. Bailey, M. R. Dietrich, J. P. Greene, W. Jiang, N. D. Lemke, Z.-T. Lu, P. Mueller, and T. P. O'Connor, Phys. Rev. Lett. **113**, 033003 (2014).
[16]K. Beloy, J. A. Sherman, N. D. Lemke, N. Hinkley, C. W. Oates, and A. D. Ludlow, Phys. Rev. A **86**, 051404 (2012).
[17]C.-Y. Xu, personal communication (2015).
[18]C. V. Ciobanu, C.-Z. Wang, and K.-M. Ho, *Atomic Structure Prediction of Nanostructures, Clusters and Surfaces* (Wiley-VCH Verlag GmbH & Co. KGaA, 2013).
[19]S. Kirkpatrick, C. D. Gelatt, Jr., and M. P. Vecchi, Science **220**, 671 (1983).
[20]Y. Wang and M. Dolg, Theor. Chem. Acc. **100**, 124 (1998).
[21]D. E. Woon and T. H. Dunning, Jr., J. Chem. Phys. **98**, 1358 (1993).
[22]S. M. Cybulski and R. R. Toczyłowski, J. Chem. Phys. **111**, 10520 (1999).
[23]P. J. Knowles, C. Hampel, and H.-J. Werner, J. Chem. Phys. **99**, 5219 (1993).
[24]P. J. Knowles, C. Hampel, and H.-J. Werner, J. Chem. Phys. **112**, 3106 (2000).
[25]S. F. Boys and F. Bernardi, Mol. Phys. **19**, 553 (1970).
[26]H.-J. Werner and P. J. Knowles, J. Chem. Phys. **89**, 5803 (1988).
[27]M. Dolg, H. Stoll, and H. Preuss, J. Chem. Phys. **90**, 1730 (1989).
[28]X. Cao and M. Dolg, J. Mol. Struct.: THEOCHEM **581**, 139 (2002).
[29]A. A. Buchachenko, G. Chałasiński, and M. M. Szczęśniak, Struct. Chem. **18**, 769 (2007).
[30]H.-J. Werner, P. J. Knowles, G. Knizia *et al.*, MOLPRO, version 2010.1, a package of *ab initio* programs, 2010, see http://www.molpro.net.
[31]R. A. Aziz, J. Chem. Phys. **99**, 4518 (1993).
[32]O. G. Peterson, D. N. Batchelder, and R. O. Simmons, Phys. Rev. **172**, 934 (1968).
[33]L. A. Schwalbe, R. K. Crawford, H. H. Chen, and R. A. Aziz, J. Chem. Phys. **66**, 4493 (1977).
[34]K. Rościszewski, B. Paulus, P. Fulde, and H. Stoll, Phys. Rev. B **62**, 5482 (2000).
[35]G. H. Jeong and K. J. Klabunde, J. Chem. Phys. **91**, 1958 (1989).
[36]S. L. Laursen and H. E. Cartland, J. Chem. Phys. **95**, 4751 (1991).
[37]O. Byrne, B. Davis, and J. G. McCaffrey, J. Chem. Phys. **142**, 054307 (2015).
[38]W. E. Klotzbucher, M. A. Petrukhina, and G. B. Sergeev, J. Phys. Chem. A **101**, 4548 (1997).
[39]M. A. Collier and J. G. McCaffrey, J. Chem. Phys. **119**, 11888 (2003).
[40]S. G. Porsev, Yu. G. Rakhlina, and M. G. Kozlov, Phys. Rev. A **60**, 2781 (1999).